Aeolian Changes at the InSight Landing Site on Mars: Multi-instrument Observations

Charalambous C.[1], McClean J. B.[1], Baker M.[2], Pike W. T.[1], Golombek M.[3], Lemmon M.[4], Ansan V.[5], Perrin C.[6], Spiga A.[7,8], Lorenz R.[9], Banks M. E.[10], Rodriguez S.[6], Murdoch N.[11], Weitz C. M.[12], Grant J. A. [14], Warner N. H.[15], Daubar I. J.[13], Hauber E.[16], Stott A. E.[1], Johnson C. L.[17,18], Mittelholz A.[17], Warren T.[19], Navarro S.[20], Sotomayor L. M.[20], Maki J.[3], Lucas A.[6], Banfield D.[21], Newman C.[22], Viúdez-Moreiras D.[20], Pla-García J.[20], Lognonné P.[6], Banerdt W. B.[3]

[1]Imperial College London, *Department of Electrical and Electronic Engineering, South Kensington Campus, Exhibition Road, SW7 2AZ, United Kingdom*

[2]Johns Hopkins University, *Morton K. Blaustein Department of Earth and Planetary Sciences, 301 Olin Hall, 3400 N. Charles St, Baltimore, MD 21218, USA*

[3]Jet Propulsion Laboratory, California Institute of Technology, *Pasadena, CA 91109, USA*

[4]Space Science Institute, *Boulder, CO, USA*

[5]Laboratoire de Planétologie et Géodynamique, UMR6112-CNRS, Univ. Nantes, *2 rue de la Houssinière, BP 92208, 44322 Nantes Cedex 3, France*

[6]Université de Paris, Institut de physique du globe de Paris, CNRS, *F-75005 Paris, France*

[7]Laboratoire de Météorologie Dynamique / Institut Pierre-Simon Laplace (LMD/IPSL), Sorbonne Université, Centre National de la Recherche Scientifique (CNRS), École Polytechnique,École Normale´ Supérieure (ENS), *Campus Pierre et Marie Curie BC99, 4 place Jussieu 75005 Paris, France*

[8]Institut Universitaire de France, *1 rue Descartes, Paris, France*

[9]Johns Hopkins Applied Physics Laboratory, *11100 Johns Hopkins Road, Laurel, MD 20723, USA*

[10]NASA Goddard Space Flight Center, *8800 Greenbelt Road, Greenbelt, MD 20771, USA*

[11]Institut Supérieur de l'Aéronautique et de l'Espace (ISAE-SUPAERO), *10 Avenue Edouard Belin, 31400 Toulouse, France*

[12]Planetary Science Institute, *1700 E Fort Lowell, Suite 106, Tucson, AZ 85719, USA*

[13]Brown University, Department of Earth, Environmental, and Planetary Sciences, *Campus Box 1846, Providence, RI 02912-1846, USA*

[14]Smithsonian Institution, *Center for Earth and Planetary Studies, National Air and Space Museum, 600 Independence Ave. SW, Washington, DC 20560, USA*

[15]State University of New York at Geneseo, Department of Geological Sciences, *1 College Circle, Geneseo, NY 14454, USA*

[16] German Aerospace Center, Institute of Planetary Research, *Rutherfordstr. 2, 12489 Berlin, Germany*

[17]University of British Columbia, *Department of Earth, Ocean and Atmospheric Sciences, Vancouver, BC, V6T 1Z4, Canada*

[18]Planetary Science Institute, 1700 East Fort Lowell, *Suite 106, Tucson, AZ 85719 USA*

[19]University of Oxford, *University of Oxford, Department of Physics, Parks Road, Oxford OX1 3PU, UK*

[20]Centro de Astrobiologíaa (CSIC-INTA), *Torrejón de Ardoz, Madrid, Spain*

[21]Cornell University, *Cornell Center for Astrophysics and Planetary Science, Ithaca, NY, 14853, USA*

[22]Aeolis Research, *333 N Dobson Road, Unit 5, Chandler AZ 85224-4412, USA*

Key Points:

- Aeolian activity at the InSight landing site is observed using simultaneous imaging and meteorological, seismological, and magnetic measurements for the first time on Mars
- Infrequent episodes of creep, dust lifting and possible saltation coincide with passage of convective vortices in the early afternoon
- Excursions in both seismic and magnetic signals correlate with aeolian changes, suggesting vortex-induced ground movement and charged-particle motion

Abstract

Orbital and surface observations demonstrate that aeolian activity is occurring on Mars. Here we report the most prominent aeolian changes observed in situ by NASA's InSight lander during the first 400 sols of operations. Aeolian changes include granule creep, dust removal with dark trails left by passing vortices, and possible saltation. InSight has observed such changes by using, for the first time, simultaneous imaging and continuous, high-frequency meteorological, seismological, and magnetic measurements. We show this multi-instrument combination constrains both the timing, and specific atmospheric conditions during which, aeolian changes occur. The observed changes are infrequent and episodic, consistently occur between noon and 3 pm, and are systematically associated with the passage of convective vortices. The sudden onset of peak vortex wind speeds promotes particle motion during sequences of enhanced vortex activity and stronger ambient winds. Aeolian changes are further correlated with excursions in ground acceleration and magnetic field strength, suggesting vortex-induced ground deformation and charged-particle motion.

Plain Language Summary

Aeolian activity, the movement of dust and sand by the wind, is common on Earth and has been observed on other planets, including Mars. A new Mars lander, InSight, has for the first time monitored aeolian changes at its landing site by combining simultaneous imaging and continuous, high-frequency meteorological, seismological, and magnetic measurements. These changes include sand grains moving along the ground and dust being lifted from both artificial and natural surfaces. InSight was also able to exploit the synergistic effects of its multi-instrument measurements to determine the timing of these changes. Although they were rare, the aeolian changes almost always happened in the early afternoon when tornado-like phenomena, called convective vortices, passed by the lander, sometimes leaving surface trails behind. The combination of the background wind speed and the rotational wind speed within a vortex was likely to be high enough to detach particles from the surface and set them into motion. When these convective vortices passed by the lander, the seismometer measured a change in ground tilt, and the magnetic field strength changed, indicating charged-particle motion during these dust lift-off events.

1 Introduction

Wind is one of the most important geomorphological agents on present-day Mars (Bridges et al., 2012). Evidence of aeolian activity includes dunes, ripples, wind streaks, and sediment-filled impact craters. Dust particles can enter into long-term suspension, influencing weather and climate through changes in the radiative balance (Gierasch and Goody, 1972; Madeleine et al. 2011). Dust deposition on solar arrays reduces power output, and wind-blown surface material can damage instruments, presenting a hazard to future human exploration (Hecht et al., 2017).

The role that wind-driven processes play in the geomorphology of Mars is complex and only partially understood, in particular the mechanism of aeolian transport and the initiation and sustenance of particle motion (Kok et al., 2012). Aeolian change is initiated when a particle detaches from the surface due to a wind shear above the fluid threshold. Detachment is the prerequisite to any subsequent motion: suspension, saltation (particles lofting followed by re-impact(s)), reptation (low-energy hopping particles), and creep (grains continuously coupled to the surface).

Due to the low density of Mars' atmosphere, the fluid threshold is higher than on Earth (Bagnold 1941; Iversen & White 1982; Newman et al., 2002). The wind shear predicted by atmospheric models (Lapotre et al., 2016), and measured on the surface, rarely exceeds this higher fluid threshold (Kok et al., 2012), yet aeolian features and dust suspension are observed (Greeley et al., 2003).

Images from surface cameras have captured evidence of sand transport (Moore et al., 1985, Sullivan et al., 2008, Baker et al., 2018). Redistribution of surface dust and active dust devils (DD) have also been observed from the surface and orbit, demonstrating that dust, with a significantly higher fluid threshold than sand, is also mobilized on Mars (Arvidson et al., 1983, Metzger et al., 1999, Greeley et al., 2010, Ellehoj et al., 2010). However, although landed spacecraft have observed motion of surface materials, very few observations had overlapping wind speed measurements needed to address aeolian transport dynamics (Geissler et al., 2010).

In November 2018, The Interior Exploration using Seismic Investigations, Geodesy and Heat Transport (InSight) mission landed in a degraded impact crater (Homestead Hollow) in western Elysium Planitia (Golombek et al., 2020, Warner et al., 2020). InSight is a geophysics mission with a seismometer, SEIS (Seismic Experiment for Interior Structure, Lognonné et al., 2019), as its primary instrument. To distinguish between seismic signals and atmospherically-induced noise, InSight measures multiple environmental parameters continuously using the Auxiliary Payload Sensor Suite (APSS, Banfield et al. 2019): wind speed and direction, temperature, pressure, and the vector magnetic field. Two cameras provide regular imaging of the surface, allowing for change detection. Hence, InSight can monitor aeolian changes with combined imaging and meteorological measurements (Spiga et al 2018).

2 Data and Methods

Aeolian changes were identified by comparing images returned from InSight's fixed Instrument Context Camera (ICC) and robot-arm-mounted Instrument Deployment Camera (IDC), capable of sampling at a scale of 0.53 mm/pixel at 0.65 m from the surface (Maki et al., 2018). Pairs of images taken under similar lighting conditions and Local Mean Solar Time (LMST) were selected whenever possible to avoid false positives caused by shadowing. These were compared by eye and image differencing (Suppl.6) to identify more subtle changes. When available, a third image, ideally taken by the IDC, was used to confirm the occurrence of an aeolian change.

SEIS and APSS measurements provided ground acceleration, wind speed and direction, pressure drop (ΔP) and vector magnetic fields. The maximum wind speed and ΔP between the image-bracketed period were noted. Passing convective vortices were recognised by the synchrony of an abrupt pressure drop, ground deformation detected by SEIS, increase in wind speed, and shifts in wind direction, including reversals.

3 Aeolian changes

Several types of aeolian change were observed including: 1) dust removal from spacecraft components, 2) granule creep and pile collapse on the surface, 3) surface dust-coating removal, 4) DD track formation, and 5) dark spots. Multi-instrument data, movies and catalogue for each change can be found in the supplement.

3.1 Spacecraft components

3.1.1 Removal of dust patch on west lander footpad

During landing the west lander footpad was partially covered with regolith and a patch of fine sediment on its east side, as observed by the IDC on Sol (S) 10. This patch was episodically removed between image pairs on S18-S20, S26-S26, and S65-S66.

The evolution of the patch is illustrated in Fig. 1a, with evidence of an ellipsoidal streak transporting along the footpad between S18-S20 (Fig. 1c, Suppl.Fig.2), likely from a wind peak of 23.6 ms^{-1} or the maximum ΔP=5.8 Pa vortex on S19 (Suppl.Fig.4). The second episodic removal occurred on S26 between 11:02-15:52 LMST containing the third-strongest wind gust in the 400-sol investigation, of 28.2 ms^{-1}, associated with a ΔP=4.1 Pa vortex (Suppl.Fig.5). The final change occurred on S65, after the incidence of a ΔP=9.2 Pa vortex inducing a wind speed of 20.1 ms^{-1}, described in Section 3.1.4. The remnant of the original dust patch, as well as the displaced ellipsoid were both removed.

3.1.2 Changes on the ICC lens

Dust particles were deposited onto the ICC lens, transferred from the protective cap opening on S4 (Fig. 1b). These were gradually removed, with the most significant cleaning observed during the first 66 sols, as illustrated by image differencing in Fig. 1b. Matched peak wind speeds ranged from 15–28 ms^{-1} with an average of 21 ms^{-1} and ΔP's ranging from 0.8–9.2 Pa. Lens cleaning events are consistently associated with short-lived wind gusts caused by vortices, at an observed minimum speed of 15 ms^{-1}, clustered at source directions of ~140° and ~285°. The lander schematic in Fig. 2e suggests that dust was most effectively removed when the wind impinged on the lens at a glancing angle.

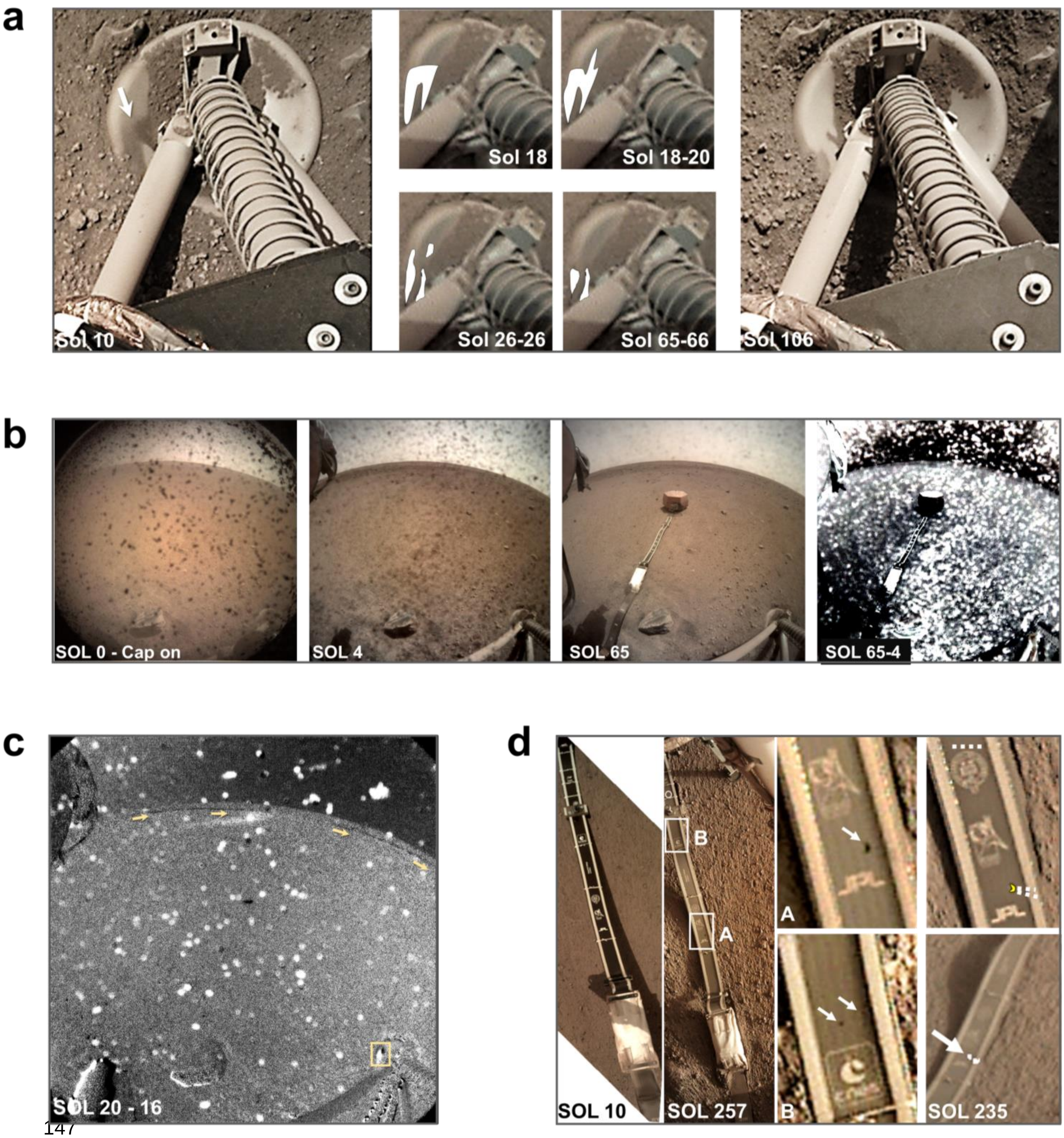

Figure 1. Spacecraft component changes: (a): IDC image of the dusty patch (arrow) on the footpad taken on S10; evolution of the patch observed by ICC images between afternoon/S18-noon/S20, noon/S26-afternoon/S26, and noon/S65-morning/S66; IDC image from S106 (b) ICC image on S0 with cap on followed by S4 after it was taken off and dust was deposited onto the lens. Right: Differencing of S65-S4. White pixels indicate the abundant dust particles removed (c) Differencing of S20-S16 demonstrates an ICC lens cleaning event (white spots across FOV), the first footpad change (rectangle) and the first likely DD track (along arrows) (d) Clean tether surface on IDC S10, vs dusty on S257. **A**, **B** show close-up views of dark spots. Note colour-similarity to clean surface. Dotted lines align to faint dark rays. (bottom right) The dark spot emerges with its rays in the overlain S237-S234 ICC differencing result (white pixels).

3.1.3 Tether

A crescent-shaped dark spot (0.5cm x 0.25cm) appeared on the tether connecting SEIS to InSight on S235, detected from ICC images taken between 08:01-15:42LMST. Conical rays extend to its right, accompanied by smaller dark spots of d<1mm and a horizontal streak (Fig. 1d). The color is consistent with the tether's dust-free surface indicating removal of localized dust deposits (Fig. 1d). The conical rays suggest that saltating particles may have impacted from the southeast, consistent with the dominant wind direction of 140° during the 8-hour image-bracketed period (Suppl.Fig.8). Data indicate a modest maximum wind speed of 17 ms^{-1} and ΔP=1.7 Pa within the image-bracketed period (Suppl.Fig.8).

3.1.4 Lander deck and solar arrays

Aeolian changes on the lander were detected with IDC images on S65 between 13:25-14:24LMST, six minutes after the largest pressure drop recorded on Mars of 9.2 Pa occurred (Banfield et al., 2020) with an associated peak wind speed of 20.1ms^{-1}– the only candidate within the image-bracketed period (Fig.2f-k, Suppl.Fig.6). Two notable changes were observed as illustrated in Fig. 2: particle motion on the Wind and Thermal Shield (WTS) and removal of a streak of dust in the lee of one of the ribs of the solar panels, associated with a 1% step increase in the solar array current (Lorenz et al., 2020). These changes likely happened simultaneously with the dust removal from the footpad (Fig. 1a). Flaky, mm-sized dust aggregates on the WTS disappeared, disaggregated or moved parallel to the streak on the arrays, in the ambient wind direction of $330^{\circ}\pm15^{\circ}$.

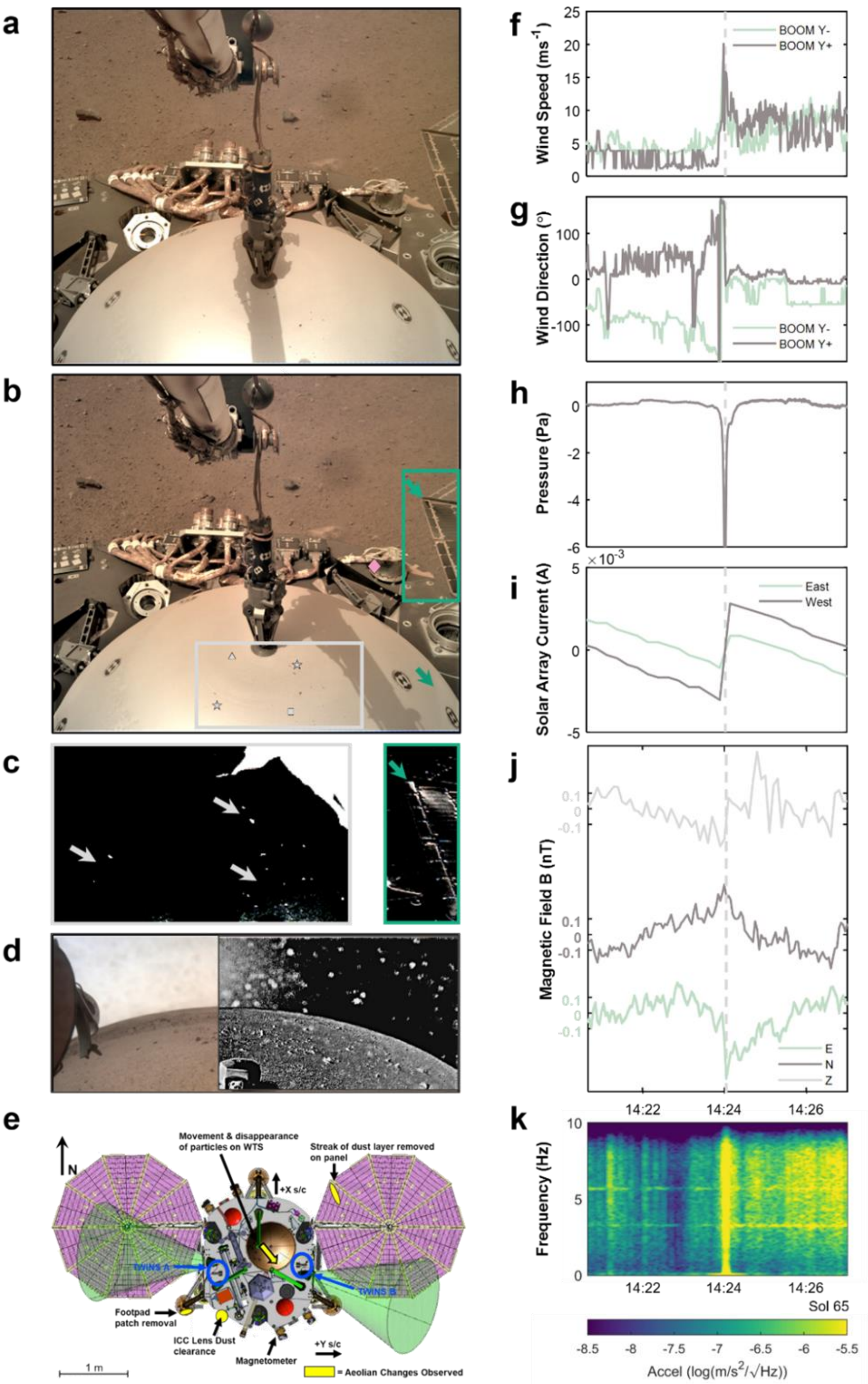

Figure 2. Observations from the largest pressure drop recorded on Mars (a) IDCs acquired on S65, 13:25 and (b) 14:24 LMST, 6 minutes after the vortex encounter. The **green** arrow shows an elongated dark streak from the dust cleaning event on the east solar panel. A particle emerges disaggregated in the measured wind direction (**square**). **Stars** mark at least four particles moving in the measured wind direction; **triangle** marks one example of disappearance; **diamond** marks multiple-grain motion on the deck (c) Differenced images of the selected areas in (b) pointing to particle motion and dust cleaning on the panel. (d) ICC lens dust cleaning in white pixels (e) Schematic of the lander indicating areas where changes were observed from the encounter (f-g) Wind speed and direction, (h) Pressure shows the vortex aligned to 180° wind-direction change, (i) Step-increase of solar array currents (j) magnetic field, indicating a link to the vortex passing, (k) Spectrogram of ZNE acceleration magnitude of the Short-Period seismometer

3.2 Surface changes

3.2.1 Near lander

Images from S362-S364 and S385-S385 show episodes of surface creep by particles of diameters up to *d*=2 mm and *d*=3 mm, respectively (Fig. 3a). In addition, motion of unresolvable sub-millimetre particles is observed, with dust aggregates appearing. IDC image differencing of S364-S362 (Suppl.Fig.9) and S385 (Fig. 3a), shows widespread subtle changes across the FOV with numerous dark spots on pebbles in the latter, indicative of dust-coating removal. A pile of regolith, originally created by the Heat Flow Probe's (HP3) tether motion during hammering, collapsed on S385 and moved parallel to the direction of particle creep. 'Splash' marks are seen in the dust on the HP3's footpad, revealing the original surface and oriented to the particle creep and wind direction, suggesting saltation occurred (Fig.3b,d). Lack of striation paths on the ground could indicate larger grains reptated (Fig.3c,e).

Further changes throughout the FOV are observed from S385-S386 ICC differencing, including cleaning of the field joint and dust-coating removal from rocks (Fig. 1b). A wide dust devil track, aligned to the ambient wind direction (~130°, SE-NW), can be seen south of the lander. ICC map-projection suggests a width of at least 5 m, with the edge approaching within 1 m of SEIS (Suppl.Fig.12). S364 estimates show the maximum wind speed observed so far at InSight at 31.6 ms^{-1}, with a ΔP=3.5 Pa (Suppl.Fig.9). A 30.5 ms^{-1} wind speed and ΔP=6 Pa were recorded on S385 between the image-bracketed period 12:00-16:00 LMST (Fig. 3g-l, Suppl.Fig.10).

3.2.2 Dust devil track formation

Dust devils (DD) are convective vortices with visible dust content (Murphy et al., 2016; Fenton et al., 2016), but 'dustless vortices' also occur (Lorenz et al., 2016). In either case, they occasionally leave tracks where surface dust has been removed (Reiss et al., 2016). InSight has detected an unprecedented level of vortex activity (Banfield, Spiga et al., 2020). Many new DD tracks were observed forming near InSight (Perrin et al., 2020) with High Resolution Imaging Science Experiment (HiRISE, McEwen et al., 2007) orbital images (0.25 m/pixel). This implies that sufficient dust removal has occurred to form tracks, yet no dust devils have been imaged by InSight's cameras (Banfield, Spiga et al., 2020), which could suggest raised dust was scarce to be visible.

Numerous newly-formed DD tracks, identified in differenced lander images, are listed in Fig. 4c, with prominent ones shown in Fig. 4b. These DD tracks are consistently oriented in the ambient wind direction and cluster in the mid-spring season, in agreement with orbital observations (Perrin et al., 2020). ICC Differencing of S18-S20 reveals the first DD track observed by InSight, likely forming on S19 from a ΔP=5.9 Pa; the same prime candidate for the footpad changes discussed in Section 3.1.1 (Fig. 1a,c).

A HiRISE image acquisition on S411 showed new tracks around the lander (Fig. 4a). The closest one (yellow arrows) is situated SW of the lander, oriented N130±2°E, with a closest approach to SEIS of ~5m. The track is at least 5m wide and formed between S384-S411. The track's azimuth and distance from the lander are consistent with the lander-imaged DD track that formed on S385 (Fig. 3f). Although the image-differenced bright zone around the lander indicates dust deposition occurred in the disturbed landing site over the period of S384-S411, ICC differencing for the same period still reveals the track (Suppl.Fig.12b). This indicates little dust deposition over this period, in agreement with the estimated erasure period of > 90 sols in the Elysium region (Reiss & Lorenz, 2016). The track is also less clearly defined near the lander: this can be explained by lack of surface dust deposits removed from the surface by the retrorockets during landing (Golombek et al., 2020). Deficiency in surface dust coatings at the site could thus account for the absence of imaged DDs by InSight's cameras.

Only two tracks were observed by both orbital and ground-based cameras; one forming on S202 (Fig 4b-top left, Banerdt et al., 2020) and another on S385, as identified in this study (Fig 4b-top

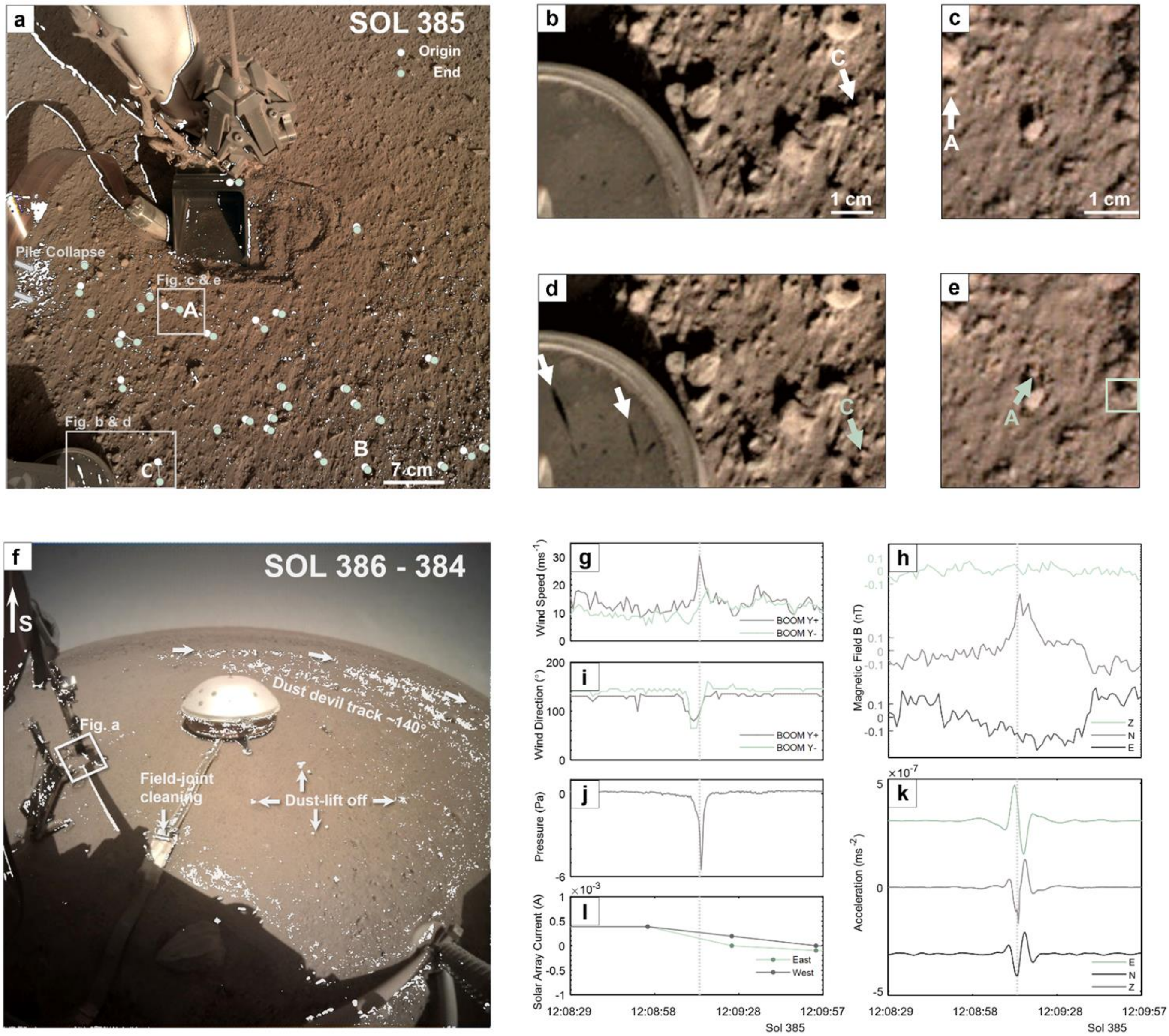

right). Other tracks observed from the ground could not be identified in HiRISE orbital images; most likely due to their small diameter and/or limited albedo contrast with the background.

Figure 3 Near-lander surface changes from S385: (a) Overlain IDC differencing (white pixels) for S385-S383. Circles represent the most robust motion identified, with origin (white) and end (green) locations. Mini mass-wasting is observed beneath the tether. Particle **A**: d=2.55 mm, moved a distance Δx=21 mm, **B**: d=2.45 mm, Δx=17 mm and **C**: d=3 mm, Δx=4 mm. (b & d) 'Splash marks' on HP3 footpad and particle **C** (c & e) Particle **A** motion and removal of dust coating (dark arrow) (f) Overlain S386-384 ICC differencing (g) Wind speed (h) Demeaned magnetic fields (i) Wind direction (j) Pressure (k) Ground acceleration band-passed 0.01<f<1 Hz, shifted +/− for E/N (l) SAC data

3.2.3 Localized dark areas

Occasionally, dark spots appear in the ICC's FOV, sometimes associated with passing vortices (Suppl.18). S385 shows such numerous dark, size-variable spots confirmed by the IDC, suggesting excess local dust deposits could be mobilized.

4 Discussion

4.3 Seismic and atmospheric synthesis

Wind and pressure measurements combined with DD track observations and ground tilt from SEIS can help constrain which convective vortex induced an observed aeolian change, a capability unique to InSight. The wind can be modelled by the superposition of a vortical flow on the ambient background wind: if the vortex passes directly over the lander, the wind speed has a double peak, while if offset from the lander, a wind peak or drop will be seen depending on whether the vortex adds or subtracts to the ambient wind measured (Ryan and Lucich, 1983, Lorenz, 2016). The S385 event shows no evidence of a double peak and the wind speed is enhanced from 12 ms^{-1} to 30.5 ms^{-1}. This implies a counterclockwise rotating vortex, consistent with a trajectory in the N130° ambient wind direction along the observed DD track and lower-bound estimations of the maximum wind in the system (Suppl.13). Assuming cyclostrophic balance, this implies a vortex diameter of <10 m passing less than one diameter from the lander.

Fitting the observed ground tilt and pressure drop to that predicted by regolith elasticity models (Lorenz et al., 2015; Murdoch et al., 2020) allows an independent determination of the DD trajectory (Fig. 1, Suppl.Fig.11). The fit validates the selection of the S385 vortex as the source with a N130° modelled trajectory matching the DD track observed both from orbit (Fig.4a) and differenced ICC map-projection (Suppl.Fig.12), as well as the observed dominant particle motion (Fig. 3a). This fit implies a vortex diameter of at least 4 m passing 5 m from the lander, consistent with the above atmospheric modelling (Suppl.13) and the map-projected differenced ICC image indicating a 4-5 m wide track at a miss-distance of 5 m from its centre (Suppl.Fig.12).

4.4 Magnetic signatures

For all near-lander observations with episodes of dust entrainment during a vortex's passage, there are associated excursions of <0.5 nT in the vector magnetic field, ***B**,* indicating a magnetic response to the vortex passing (S19-Suppl.Fig.4, S26-Suppl.Fig.5, S65-Fig.2j, S385-Fig.3h, S364-Suppl.Fig.9). This is consistent with Johnson et al. (2020) who identified small magnetic field changes (<1 nT) for 20 % of 54 identified pressure drop events in InSight data.

Assuming these are not caused by a drop in the solar array current (SAC) due to dust lifting (Fig. 2i, 3l), wind induced panel motion or other sources, they may provide a probe of the electric charge present on mobilized dust grains. This could be produced by, for example, triboelectric charging (Eden et al., 1973, Jackson et al., 2006, Farrell, 2004, Kurgansky et al., 2007). For S385, multiple peaks are observed within a predominant northerly excursion, while for S65, the maximum excursion in ***B*** occurs simultaneously with the peak wind speed, 180° wind-reversal, step change in SAC, $\underline{\Delta P}_{max}$, and maximum ground acceleration.

4.5 Fluid threshold investigation

Our observations suggest that surface material is mobilised infrequently in short-lived episodes, likely due to the superposition of high tangential wind speeds at the eyewall of strong passing vortices and generally higher ambient wind speeds (~10 ms^{-1},S19-Suppl.Fig.4,S26-Suppl.Fig.5,S364-Suppl.Fig.9,S385-Fig.3h). Fig. 4c shows a compilation of all changes and associated atmospheric conditions, temporally correlated with vortex activity, measured as the daily number of pressure excursions above 0.3 Pa, a proxy for atmospheric daytime turbulence.

Each event-associated peak wind speed, u_x, can be converted into the wind shear u^*, by assuming a logarithmic wind profile, $u^*= ku_x/\ln(z/z_0)$ (Prandtl & Tietjens 1934), where k is the von Kármán constant (0.40), z the height at which u_x is measured (1.2 m, Banfield et al., 2020), and z_0 is the aerodynamic surface roughness length (1–5 mm, Baker et al., 2020). The measured u^* can be compared to the fluid threshold u^*_T, predicted by the model of Shao & Lu (2000). The area under each curve in Fig. 4d denotes the complete set of solutions for the maximum and minimum u_x values observed to have induced surface particle detachment, for a range of z_0 and grain diameters d.

Displacement of dust from the west lander footpad (Fig. 1a), was observed only for vortex-induced u_x>20.3 ms^{-1}. For u_x=20.3 ms^{-1}, u*=1.2 ms^{-1}, and no mobilization of particles is predicted for z_0=1–5 mm. However, observations show that mobilization of particles *did* occur: dust particles, likely d<62.5 µm, were removed from the footpad. Other exceedances of this wind speed, not always associated with a pressure drop ΔP, i.e. possibly corresponding to mere turbulent gusts, did not result in dust removal, suggesting that wind speed may not be a *sufficient* condition for dust removal.

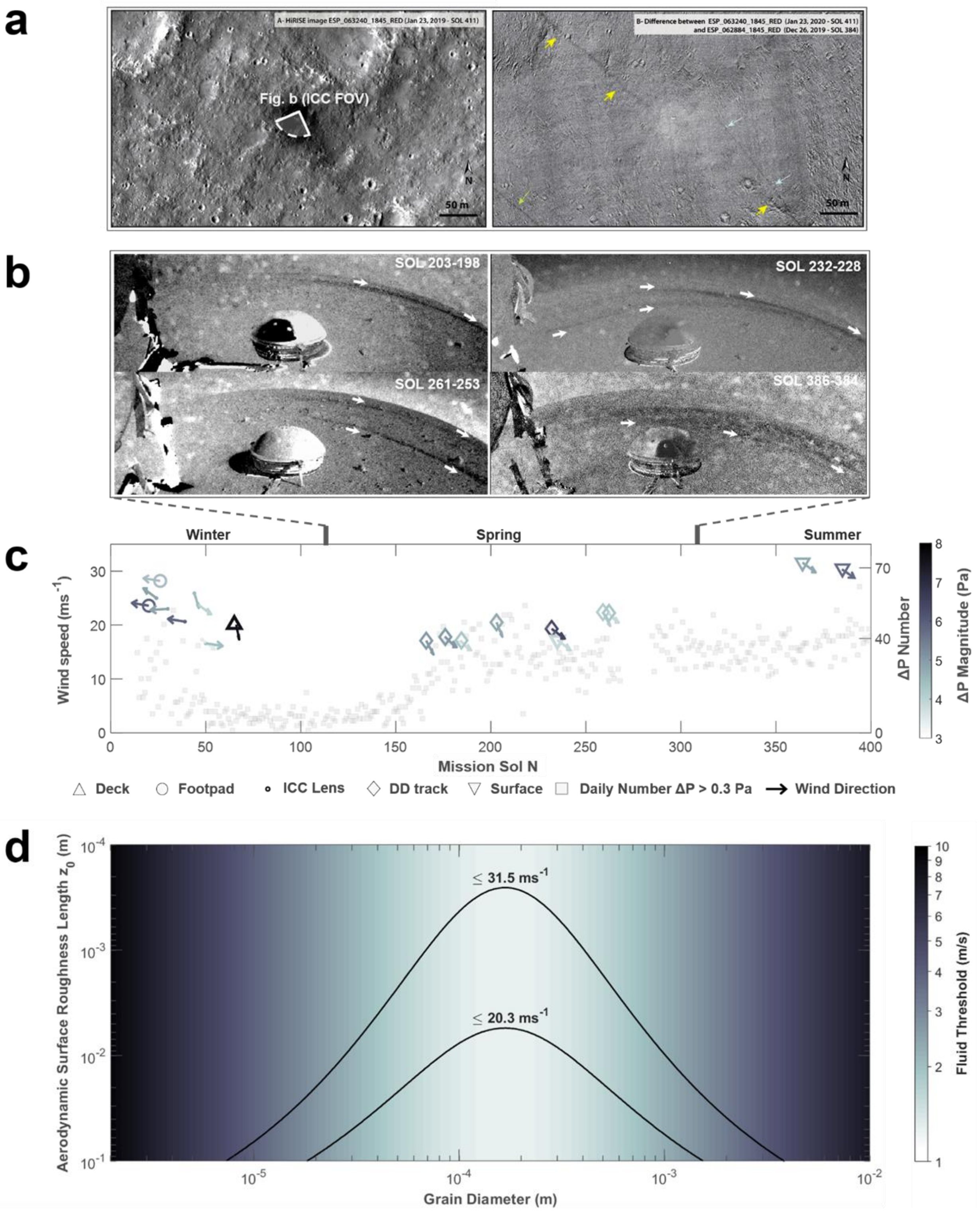

Figure 4 (a-left) HiRISE image acquired on S411, centered above InSight (dark area represents the retrorocket scour during landing), with the ICC FOV indicated. (a-right) Difference between HiRISE images (ESP_063240_1845_RED-ESP_062884_1845) presenting new dust-devil tracks (streaks highlighted by arrows) formed between S384-S411, and a bright area, indicating dust deposition. Yellow arrows indicate likely the S385 track from Section 3.2.1, also shown in Fig 3f,4b (b) Differencing of afternoon images of S203-S198, S386-384, S261-S253 and S232-S228 reveal DD tracks (b). Compilation of all changes, incorporating atmospheric conditions of the candidate vortices favored to have induced motion. Aeolian changes correlate to the daily number of pressure drops >0.3Pa, shown by squares (d) Set of solutions below the curves based on Shao & Lu (2000) model for the maximum and minimum u_x observed so far inducing particle motion

Creep and possible saltation were only observed on the two occasions when the wind speed exceeded 30 ms^{-1} (S364 and S385). Surprisingly, more aeolian changes were observed on S385 (u_x=30.5ms^{-1}) than on S364's (u_x=31.5 ms^{-1}). A larger ΔP was observed on S385 compared to S364, suggestive of a closer encounter, or a more energetic vortex, inducing higher tangential velocities and vorticity above the threshold for reliable wind speed retrieval (Suppl.Fig.13). This sets a lower bound on the S385 peak u_x that is likely to be equal to or greater than the S364 peak u_x of 31.5 ms^{-1}, for which u*=1.8 ms^{-1} for z_0=1 mm, conditions which particles between 65 and 430 μm would be expected to saltate. Further observations supporting saltation of particles include 'splash' marks from dust removal on the west HP3 footpad, lack of striation paths on the surface and disappearance of multiple, unresolvable sub-mm grains (Fig. 1b-e).

However, observations also show motion of mm-sized sand grains, above the expected saltation threshold, and dust-coating removal from rocks, with particle sizes below the threshold. The sand grains may have rolled rather than saltated, thus consistent with drag-induced rolling (Suppl.Fig.17, Merrison et al. 2007,Baker et al., 2020,). The dust coatings are likely airfall particles with d<20 μm (Johnson et al, 2002), below the predicted minimum mobilized particle size. The observed dust removal could be explained by larger z_0: to mobilize dust-sized particles with d<62.5 μm and a minimum wind speed of 20.3 ms^{-1}, as observed on the lander footpad, z_0>2 cm is required. To lift 3 μm dust-particle coatings at u_x=31.5 ms^{-1}, as observed on rocks on S385, a z_0>8 cm is required.

Estimates of z_0 are correlated with rock abundance, the percentage of the surface covered by rocks (Hebrard et al., 2012). Local rock abundance in the sand-rich Homestead Hollow is low (1.5%, Golombek et al., 2020), consistent with a z_0 of a few millimetres. Incorporating deployed instruments as roughness elements raises the local equivalent rock abundance to over 10% (Suppl.19), higher than the Viking lander 2 site (Golombek et al., 2012) with z_0=1 cm (Sutton et al., 1978). A rockier area to the west, and beyond the hollow's boundary, suggests a rock abundance of >5% (Charalambous et al., 2019). Such considerations are consistent with the location of DD tracks, with 9 of 10 observed in these rougher terrains, where higher surface-to-atmosphere exchange of mass and energy would promote dust removal. Our results suggest that z_0 at InSight could be spatially highly heterogeneous, similar to terrestrial arid areas (Marticorena et al., 2006).

Alternatively, if z_0 is indeed in the 1–5 mm range, this discrepancy in dust removal could be explained either by wind speed measurement limitations at high vorticity likely setting only a lower bound to the wind speed, or by the failure to include other detachment mechanisms not incorporated in Shao & Lu's (2000) model. These mechanisms include dust removal assisted by saltation clusters (Sullivan & Kok 2017); thermophoresis (Wurm et al., 2008); 'sandblasting' by bigger particles (Greeley 2002); electrification of particles (Neakrase et al., 2016); and the 'delta-P' (suction) effect (Balme & Greeley 2006, Baker et al., 2020).

5 Conclusion

The paucity of evidence for grain transport by free-stream winds, coupled with the bright appearance of dust-mantled bedforms and most hollows in the vicinity of Homestead hollow, suggests a largely stable surface around the InSight lander, with local, limited particle motion predominantly related to the passage of atmospheric vortices. Such an interpretation is consistent with sparse organized bedforms (Golombek et al., 2018), the lack of wind tails or ripples at the site, and the presence of a weakly cemented or duricrust layer near the top of the hollow fill that implies long term stability of the surface and sequestering of most infilling sediments (Golombek et al., 2020; Grant et al., 2020; Warner et al., 2020). Reduced energy production rates seen by the solar arrays (Lorenz et al., 2020) and HiRISE orbital image differencing (Fig.4a) provide further evidence that dust deposition may be the predominant aeolian process at InSight over the 400-sol investigation.

Given that all aeolian change events are systematically associated with large ΔPs, convective vortices appear to be the primary mechanism for dust entrainment, sporadic surface creep of grains *d*<3 mm, and likely saltation. The sudden wind peaks in wind speed induced by these passing vortices are for the first time resolved by InSight's high-frequency wind measurements, opening a unique avenue into the better understanding of vortices as an important driver of surface motion on Mars. Finally, episodic aeolian changes are correlated with excursions in both seismic and magnetic signals as might be expected from vortex-induced ground movement and charged-particle motion, respectively. Ongoing analysis should provide a further insight into atmospheric coupling with the regolith, and induced aeolian transport and its dynamics on Mars.

References

Arvidson, R. E., Guinness, E. A., Moore, H. J., Tillman, J., & Wall, S. D. (1983). Three Mars years: viking lander 1 imaging observations. *Science*, 222(4623), 463-468.

Bagnold, R. (1941). The physics of blown sand and desert dunes.

Baker, M.M., Newman, C., Charalambous, C., Golombek, M., Spiga, A., Banfield, D., Lemmon, M., Banks, M., Garvin, J., Grant, J., Lewis, K., Ansan, V., Warner, N., Weitz, C., Wilson., S., The modern aeolian environment at Homestead hollow, Mars, *JGR Planets, this issue*

Baker, M.M., Lapotre, M.G., Minitti, M.E., Newman, C.E., Sullivan, R., Weitz, C.M., Rubin, D.M., Vasavada, A.R., Bridges, N.T. and Lewis, K.W., 2018. The Bagnold Dunes in southern summer: Active sediment transport on Mars observed by the Curiosity rover. *Geophysical Research Letters*, 45(17), pp.8853-8863

Balme, M. R., & Greeley, R. (2006). Dust devils on Earth and Mars. *Reviews of Geophysics*, *44*, 3003-+. doi: 10.1029/2005RG000188

Banerdt, W. B., Smrekar, S. E., Banfield, D., Giardini, D., Golombek, M., Johnson, C. L., ... & Stähler, S. C. (2020). Initial results from the InSight mission on Mars. *Nature Geoscience*, 1-7.

Banfield, D., Spiga, A., Newman, C., Forget, F., Lemmon, M., Lorenz, R., ... & Lognonné, P. (2020). The atmosphere of Mars as observed by InSight. *Nature Geoscience*, 1-9.

Bridges, N. T., Ayoub, F., Avouac, J. P., Leprince, S., Lucas, A., & Mattson, S. (2012). Earth-like sand fluxes on Mars. *Nature*, *485*(7398), 339-342.

Clinton, J. F., Giardini, D., Lognonné, P., Banerdt, B., van Driel, M., Drilleau, M., ... & Golombek, M. (2017). Preparing for InSight: An invitation to participate in a blind test for Martian seismicity. *Seismological Research Letters*, *88*(5), 1290-1302.

Eden, H. F., & Vonnegut, B. (1973). Electrical breakdown caused by dust motion in low-pressure atmospheres: Considerations for Mars. *Science*, *180*(4089), 962-963.

Ellehoj, M. D., Gunnlaugsson, H. P., Taylor, P. A., Kahanpää, H., Bean, K. M., Cantor, B. A., ... & Holstein-Rathlou, C. (2010). Convective vortices and dust devils at the Phoenix Mars mission landing site. *Journal of Geophysical Research: Planets*, 115(E4).

Farrell, W. M. Electric and magnetic signatures of dust devils from the 2000–2001 MATADOR desert tests. J. Geophys. Res. 109,E03004 (2004).

Geissler, P. E., Sullivan, R., Golombek, M., Johnson, J. R., Herkenhoff, K., Bridges, N., Vaughan, A., Maki, J., Parker, T., and Bell, J., 2010, Gone with the Wind: Eolian erasure of the Mars rover tracks, Journal of Geophysical Research, Planets, v. 115, E00F11, doi:10.1029/2010JE003674.

Gierasch, P. J., & Goody, R. M. (1972). The effect of dust on the temperature of the Martian atmosphere. *Journal of the Atmospheric Sciences*, *29*(2), 400-402.

Golombek, M., Warner, N. H., Grant, J. A., Hauber, E., Ansan, V., Weitz, C. M., ... & Kopp, M. (2020). Geology of the InSight landing site on Mars. *Nature communications*, 11(1), 1-11.

Golombek, M., Huertas, A., Kipp, D., & Calef, F. (2012). Detection and characterization of rocks and rock size-frequency distributions at the final four mars science laboratory landing sites. *International Journal of Mars Science and Exploration*, *7*, 1–22.

Golombek, M., Kipp, D., Warner, N., Daubar, I. J., Fergason, R., Kirk, R. L., ... Banerdt, W. B. (2017). Selection of the InSight Landing Site. *Space Science Reviews*, *211*, 5-95. doi: 10.1007/s11214-016-0321-9

Golombek, M., Grott, M., Kargl, G., Andrade, J., Marshall, J., Warner, N., ... & Lichtenheldt, R. (2018). Geology and physical properties investigations by the InSight lander. *Space Science Reviews*, *214*(5), 84.

Greeley, R. (2002). Saltation impact as a means for raising dust on Mars. *Planetary and Space Science*, *50*, 151-155. doi: 10.1016/S0032-0633(01)00127-1

Greeley, R., Kuzmin, R. O., Rafkin, S. C. R., Michaels, T. I., & Haberle, R. (2003). Wind-related features in Gusev crater, Mars. *Journal of Geophysical Research (Planets)*, *108*(E12), 8077. doi: 10.1029/2002JE002006

Greeley, R., Waller, D. A., Cabrol, N. A., Landis, G. A., Lemmon, M. T., Neakrase, L. D., ... & Whelley, P. L. (2010). Gusev Crater, Mars: Observations of three dust devil seasons. *Journal of Geophysical Research: Planets*, *115*(E7).

Hebrard, E., Listowski, C., Coll, P., Marticorena, B., Bergametti, G., M¨a¨att¨anen, A., ... Forget, F. (2012). An aerodynamic roughness length map derived from extended martian rock abundance data Journal of *Geophysical Research*, *117*(E4), E04008.

Hecht, M. H., McClean, J. B., Pike, W. T., Smith, P. H., Madsen, M. B., Rapp, D., & Team, M. (2017, June). MOXIE, ISRU, and the History of In Situ Studies of the Hazards of Dust in Human Exploration of Mars. In *Dust in the Atmosphere of Mars and Its Impact on Human Exploration* (Vol. 1966).

Hess, S. L., Henry, R. M., Leovy, C. B., Ryan, J. A., & Tillman, J. E. (1977). Meteorological results from the surface of Mars: Viking 1 and 2. *J. Geophys. Res.*, *82*, 4559-4574.

Holstein-Rathlou, C., Gunnlaugsson, H. P., Merrison, J. P., Bean, K. M., Cantor, B. A., Davis, J. A., ... Taylor, P. A. (2010). Winds at the Phoenix landing site. *Journal of Geophysical Research (Planets)*, *115*(12), E00E18. doi: 10.1029/2009JE003411

InSight Mars SEIS Data Service. (2019). SEIS raw data, Insight Mission. IPGP, JPL, CNES, ETHZ, ICL, MPS, ISAE-Supaero, LPG, MFSC. https://doi.org/10.18715/SEIS.INSIGHT.XB_2016Iversen, J. D., & White, B. R. (1982). Saltation threshold on earth, mars and venus. *Sedimentology*, *29*(1), 111–119.

Jackson, T. L. & Farrell, W. M. Electrostatic fields in dust devils: an analog to Mars. *IEEE Trans. Geosci. Remote Sens*. 44, 2942–2949 (2006).

Johnson, C. L., Mittelholz, A., Langlais, B., Russell, C. T., Ansan, V., Banfield, D., ... & Golombek, M. (2020). Crustal and time-varying magnetic fields at the InSight landing site on Mars. *Nature Geoscience*, *13*(3), 199-204.

Kok, J. F., Parteli, E. J., Michaels, T. I., & Karam, D. B. (2012). The physics of wind-blown sand and dust. *Reports on progress in Physics*, *75*(10), 106901.

Kurgansky, M. V., Baez, L. & Ovalle, E. M. A simple model of the magnetic emission from a dust devil. J. Geophys. Res. 112, E11008 (2007).,

Lapotre, M., Ewing, R., Lamb, M., Fischer, W., Grotzinger, J., Rubin, D., ... others (2016). Large wind ripples on mars: A record of atmospheric evolution. *Science*, *353*(6294), 55–58.

Lognonné, P., Banerdt, W. B., Giardini, D., Pike, W. T., Christensen, U., Laudet, P., ... & Hurst, K. J. (2019). SEIS: Insight's seismic experiment for internal structure of Mars. *Space Science Reviews*, 215(1), 12.
Lorenz, R.D., 2016. Heuristic estimation of dust devil vortex parameters and trajectories from single-station meteorological observations: Application to InSight at Mars. Icarus, 271, pp.326-337

Lorenz, e. a., R. (2020). Scientific Observations with the InSight Solar Arrays : Dust, Clouds and Eclipses on Mars. *this issue*.

Madeleine, J. B., Forget, F., Millour, E., Montabone, L., & Wolff, M. J. (2011). Revisiting the radiative impact of dust on Mars using the LMD Global Climate Model. *Journal of Geophysical Research: Planets*, *116*(E11).

Maki, J. N., Golombek, M., Deen, R., Abarca, H., Sorice, C., Goodsall, T., ... Banerdt, W. B. (2018, Aug 29). The color cameras on the insight lander. *Space Science Reviews*, *214*(6), 105. Retrieved from https://doi.org/10.1007/ s11214-018-0536-z doi: 10.1007/s11214-018-0536-z

Marticorena, B., Kardous, M., Bergametti, G., Callot, Y., Chazette, P., Khatteli, H., ... others (2006). Surface and aerodynamic roughness in arid and semiarid areas and their relation to radar backscatter coefficient. *Journal of Geophysical Research: Earth Surface*, *111*(F3).

McEwen, A. S., Eliason, E. M., Bergstrom, J. W., Bridges, N. T., Hansen, C. J., Delamere, W. A., et al. (2007). Mars reconnaissance orbiter's high resolution imaging science experiment (HiRISE). *Journal of Geophysical Research E: Planets*, *112*(5), 1–40. https://doi.org/10.1029/2005JE002605

Merrison, J. P., Gunnlaugsson, H. P., Nørnberg, P., Jensen, A. E., & Rasmussen, K. R. (2007). Determination of the wind induced detachment threshold for granular material on mars using wind tunnel simulations. *Icarus*, *191*(2), 568–580.

Metzger, S. M., Carr, J. R., Johnson, J. R., Parker, T. J., & Lemmon, M. T. (1999). Dust devil vortices seen by the Mars Pathfinder camera. Geophysical research letters, 26(18), 2781-2784.

Newman, C. E., S. R. Lewis, P. L. Read, and F. Forget, Modeling the Martian dust cycle, 1, Representations of dust transport processes, J. Geophys. Res., 107(E12), 5123, doi:10.1029/2002JE001910, 2002.

Newman, C. E., Gómez-Elvira, J., Marin, M., Navarro, S., Torres, J., Richardson, M. I., ... & Vasavada, A. R. (2017). Winds measured by the Rover Environmental Monitoring Station (REMS) during the Mars Science Laboratory (MSL) rover's Bagnold Dunes Campaign and comparison with numerical modeling using MarsWRF. *Icarus*, *291*, 203-231.

Perrin, C., Rodriguez, S., Jacob, A., Lucas, A., Spiga, A., Murdoch, N., et al. (2020). Monitoring of Dust-Devil Tracks Around the InSight Landing Site, Mars, and Comparison with in-situ Atmospheric Data. *Geophysical Research Letters*, *this issue*.

Prandtl, L., & Tietjens, O. G. (1934). *Applied hydro- and aeromechanics*. New-York: Dover Publications, Inc.

Ryan, J.A. and Lucich, R.D., 1983. Possible dust devils, vortices on Mars. Journal of Geophysical Research: Oceans, 88(C15), pp.11005-11011.

Schofield, J. T., Crisp, D., Barnes, J. R., Haberle, R. M., Magalhaes, J. A., Murphy, J. R., ... Wilson, G. (1997). The Mars Pathfinder Atmospheric Structure Investigation/Meteorology (ASI/MET) experiment. *Science*, *278*, 1752-1757.

Shao, Y., & Lu, H. (2000). A simple expression for wind erosion threshold friction velocity. *Journal of Geophysical Research: Atmospheres*, *105*(D17), 22437–22443.

Sullivan, R., & Kok, J. (2017). Aeolian saltation on mars at low wind speeds. *Journal of Geophysical Research: Planets*, *122*(10), 2111–2143.

Sutton, J. L., Leovy, C. B., & Tillman, J. E. (1978). Diurnal variations of the Martian surface layer meteorological parameters during the first 45 sols at two Viking lander sites. *J. Atmos. Sci.*, *35*, 2346-2355.

Wurm, G., Teiser, J., & Reiss, D. (2008). Greenhouse and thermophoretic effects in dust layers: The missing link for lifting of dust on mars. *Geophysical Research Letters*, *35*(10).